Journal of Natural Gas Science and Engineering 71 (2019) 102973

Contents lists available at ScienceDirect

Journal of Natural Gas Science and Engineering

journal homepage: www.elsevier.com/locate/jngse

A compositional model for gas injection IOR/EOR in tight oil reservoirs under coupled nanopore confinement and geomechanics effects

Ye Tian[a], Yi Xiong[a], Lei Wang[b], Zhengdong Lei[c], Yuan Zhang[c], Xiaolong Yin[a], Yu-Shu Wu[a,*]

[a] Colorado School of Mines, Golden, CO 80401, USA
[b] Nazarbayev University, Nur-Sultan 010000, Kazakhstan
[c] Research Institute of Petroleum Exploration and Development, PetroChina, Beijing 100083, China

ARTICLE INFO

Keywords:
Gas injection
EOR
Compositional modeling
Tight oil reservoirs
Geomechanics
Nanopore confinement

ABSTRACT

The nanopore confinement and geomechanics are generally considered as non-negligible in tight oil reservoirs, but their coupled effects are still not well understood for gas injection which is becoming a favorable Improved/Enhanced Oil Recovery (IOR/EOR) technique for tight oil. We present a general compositional model to investigate the complex multiphase and multicomponent behaviors under coupled nanopore confinement and geomechanics in tight oil reservoirs. The in-house simulator developed is validated against a commercial simulator before being applied to simulate dry gas huff-n-puff in Eagle Ford. The simulation reveals that huff-n-puff would improve the recovery factor (RF) of each component versus the depletion. If the reservoir pressure is much higher than the bubble point, the nanopore confinement will have a minimal impact on RF for both the depletion and early cycles of huff-n-puff. Geomechanics is found to be an important factor for RF but not always detrimental, as enhanced compaction drive of matrix could offset the permeability reduction of fracture in certain scenarios. The heavy component would first have a higher RF than the light component in early huff-n-puff cycles, but its RF will be gradually outpaced by the light and finally surpassed after a crossover point which is controlled by the critical gas saturation of matrix. Considering the nanopore confinement in the simulation will delay this crossover and reduce the RF of the light component but increase the RF of the heavy component after huff-n-puff. This work can better assist engineers to understand the complex multiphase and multicomponent behaviors during gas injection in tight oil reservoirs.

1. Introduction

In 2018, about 61% of the total oil produced in the United States was attributed to tight oil reservoirs, and this number is predicted to reach 70 % in the 2030s (EIA, 2019). Unconventional oil producing basins such as Bakken, Eagle Ford, Permian, and Niobrara have drawn significant attention within the global oil industry over the last decade. Currently, the best practice to produce tight oil is through primary depletion using multistage hydraulically fractured horizontal wells, but the recovery factors are low, typically below 10% (Hoffman and Evans, 2016) due to the nature of unconventional reservoirs. For example, in Bakken despite the application of horizontal drilling and multistage hydraulic fracturing, the oil recovery factor is still about 4–6% (Hawthorne et al., 2013). Also, unconventional oil wells are characterized by a fast decline rate between 50% and 70% during the first year of production (Wang et al., 2017). With the large volume of oil in place in unconventional reservoirs, e.g., a proven oil reserve of 2.3 billion barrels in Eagle Ford (Gong et al., 2013), the success of IOR/EOR practice with even a minor improvement of 1% would lead to an enormous increase in oil production.

Over the past few years, many methods have been proposed for IOR/EOR in tight oil reservoirs based on theoretical research and laboratory studies (Kurtoglu et al., 2013; Gamadi et al., 2014), some of which were applied in pilot tests (Sheng, 2015). So far, the most promising IOR/EOR technologies for tight oil reservoirs seems to be gas injection (hydrocarbon gas, CO_2, N_2, etc.), because gas often has a higher compressibility and a lower viscosity than liquid, leading to higher injectivity and energy supplement potentials for tight formations. Immiscible gas injection can supply reservoir with additional energy meanwhile the dissolution of injected gas can also swell the oil and reduce its viscosity (Peng et al., 2017). For a miscible flood, the interfacial tension (IFT) between injected gas and oil could be significantly lowered even eliminated which would dramatically increase microscopic displacement efficiency in addition to the mechanism of an

* Corresponding author.
E-mail addresses: yetian@mines.edu (Y. Tian), ywu@mines.edu (Y.-S. Wu).

https://doi.org/10.1016/j.jngse.2019.102973
Received 30 January 2019; Received in revised form 26 July 2019; Accepted 18 August 2019
Available online 23 August 2019
1875-5100/ © 2019 Elsevier B.V. All rights reserved.

immiscible process. Lastly, for tight reservoirs, gas injection often causes less formation damage than liquid injection. Therefore, injection with either hydrocarbon or non-hydrocarbon gas has become the top choice for IOR/EOR pilots in unconventional reservoirs. Gas huff-n-puff is often favored compared with flooding because of the easiness as a single-well operation and a short response time (Wang et al., 2017).

Though a black oil model could be implemented for modeling IOR/EOR in tight oil reservoirs such as water flood or immiscible gas injection, compositional modeling based on an equation of state (EOS) is becoming a favored approach in most recent published studies. This is mainly because black oil models could not accurately handle the transport process (Qiao, 2015) when it is highly compositional dependent or when capillary confinement might shift the Vapor-Liquid Equilibrium (VLE), let alone when these effects are coupled with geomechanics. Several compositional models for tight oil reservoirs considering complex physics have been established, but they mainly focused on primary depletion (Xiong, 2015; Uzun et al., 2018). Many simulation studies for gas EOR in tight oil reservoirs have been done, but most of them are either based on conventional compositional models (Chen et al., 2014; Wan et al., 2016) or commercial software (Hoffman et al., 2014; Sheng and Chen, 2014; Sanchez-Rivera et al., 2015; Yu et al., 2015; Phi and Schechter, 2017) where the effects of complex physics are less studied, e.g., coupled stress and capillary confinement effects. This paper presents a fully-implicit compositional model that couples nanopore confinement and geomechanical effects during gas injection in tight oil reservoirs. Simulation results from this model reveal some insightful multiphase and multicomponent behaviors, which could only be understood using a compositional simulator with coupled nanopore confinement and geomechanics.

2. Compositional modeling

The compositional model in this paper is based on the framework initially developed by Wu (2015); Xiong (2015). $Nc + 1$ mass balance equations correspond with $Nc + 1$ components. Among them, Nc equations are for the components existing in both oil and gas phases which can be pure hydrocarbon, non-hydrocarbon (e.g., CO_2 or N_2) or pseudo components as long as the thermodynamic properties required by EOS are specified.

$$-\nabla\cdot(\rho_o x_i \vec{v}_o + \rho_g y_i \vec{v}_g) + \nabla\cdot[D_{\mathrm{eff},i}\nabla(\rho_g y_i)] + q_i = \frac{\partial[\phi(\rho_o S_o x_i + \rho_g S_g y_i)]}{\partial t} \tag{1}$$

The last mass balance equation is for the water component, which is assumed to be present only in the aqueous phase.

$$-\nabla\cdot(\rho_w \vec{v}_w) + q_w = \frac{\partial(\phi\rho_w S_w)}{\partial t} \tag{2}$$

These partial differential equations are integrated within the arbitrary representative elementary volume (REV) by following the integral finite difference (IFD) method, which is essentially equivalent to the finite volume method (Pruess, 1991).

$$\int_{V_n} -\nabla\cdot(\rho_o x_i \vec{v}_o + \rho_g y_i \vec{v}_g)\mathrm{d}V + \int_{V_n} \nabla\cdot[D_{\mathrm{eff},i}\nabla(\rho_g y_i)]\mathrm{d}V + \int_{V_n} q_i \mathrm{d}V = \int_{V_n} \frac{\partial[\phi(\rho_o S_o x_i + \rho_g S_g y_i)]}{\partial t}\mathrm{d}V \tag{3}$$

where V_n represents the volume of a grid block. By applying the divergence theorem, volume integrals are converted to surface integrals.

$$\int_{S_n} -(\rho_o x_i \vec{v}_o + \rho_g y_i \vec{v}_g)\cdot\hat{n}\mathrm{d}S + \int_{S_n} D_{\mathrm{eff},i}\nabla(\rho_g y_i)\cdot\hat{n}\mathrm{d}S + \int_{V_n} q_i \mathrm{d}V = \int_{V_n} \frac{\partial[\phi(\rho_o S_o x_i + \rho_g S_g y_i)]}{\partial t}\mathrm{d}V \tag{4}$$

where S_n denotes the surface area of a grid block, and $\hat{n}$ is the outward normal unit vector that describes the spatial orientation of dS. Fluids and rock properties are evaluated by averaging them over explicitly defined grid blocks, while mass fluxes across the interface between neighboring grids are approximated by the finite difference method. Discretization of time is implemented with the backward first-order finite difference approximation. Upstream mobility weighting is implemented. Finally, the discretized equations are written into a residual form and ready to be solved by Newton iterations.

$$\begin{aligned} R_{i,n}^{t+1} = {} & \frac{[V_n\phi(\rho_o S_o x_i + \rho_g S_g y_i)]_n^{t+1} - [V_n\phi(\rho_o S_o x_i + \rho_g S_g y_i)]_n^t}{\Delta t} \\ & - \sum_{m\in\eta_n}[(\rho_o x_i\lambda_o)_{nm+1/2}^{t+1}\gamma_{nm}^{t+1}(\Phi_{om}^{t+1} - \Phi_{on}^{t+1}) \\ & + (\rho_g y_i\lambda_g)_{nm+1/2}^{t+1}\gamma_{nm}^{t+1}(\Phi_{gm}^{t+1} - \Phi_{gn}^{t+1})] \\ & - \sum_{m\in\eta_n}\left[D_{eff,i}A_{nm}^{t+1}\frac{(\rho_g y_i)_m^{t+1} - (\rho_g y_i)_n^{t+1}}{d_n^{t+1} + d_m^{t+1}}\right] - (V_n q_i)_n^{t+1} \end{aligned} \tag{5}$$

Similarly, the residual form of mass balance equation for aqueous phase can be written as,

$$\begin{aligned} R_{w,n}^{t+1} = {} & \frac{[V_n\phi\rho_w S_w]_n^{t+1} - [V_n\phi\rho_w S_w]_n^t}{\Delta t} \\ & - \sum_{m\in\eta_n}[(\rho_w\lambda_w)_{nm+1/2}^{t+1}\gamma_{nm}^{t+1}(\Phi_{wm}^{t+1} - \Phi_{wn}^{t+1})] - (V_n q_w)_n^{t+1} \end{aligned} \tag{6}$$

where the transmissibility γ_{nm} between two connected grids is defined as,

$$\gamma_{nm}^{t+1} = \left(\frac{A_{nm}k_{nm+1/2}}{d_n + d_m}\right)^{t+1} \tag{7}$$

where A_{nm} is the interface area between connected grid n and m; d_n is the distance from the center of grid n to the interface between grid n and m as shown in Fig. 1; $k_{nm+1/2}$ is the harmonically averaged absolute permeability along the connection between grid n and m.

2.1. Geomechanics

The geomechanical formulation in this study is based on the previous work by Winterfeld and Wu (2016). From the classical poro-thermal-elastic theory, we can write

$$\boldsymbol{\sigma} - \alpha p\mathbf{I} - 3\beta K\Delta T = 2G\boldsymbol{\varepsilon} + \lambda(tr\boldsymbol{\varepsilon})\mathbf{I} \tag{8}$$

where $\boldsymbol{\sigma}$ is the stress tensor; $\mathbf{I}$ is the identity matrix; α is Biot's coefficient; β is the linear thermal expansion coefficient; K is the bulk modulus; G is shear modulus; λ is Lame's first parameter. Also, we have the relationship between the displacement vector $\vec{u}$ and the strain tensor $\boldsymbol{\varepsilon}$ as,

$$\boldsymbol{\varepsilon} = \frac{1}{2}[\nabla\vec{u} + (\nabla\vec{u})^{\mathrm{T}}] \tag{9}$$

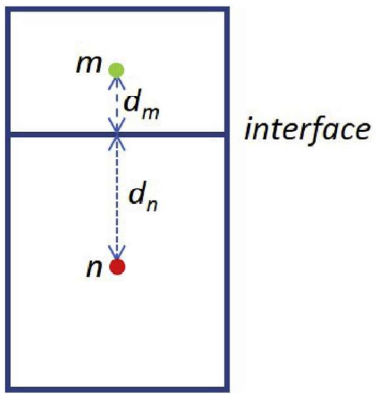

Fig. 1. Connection between two neighboring grids.

Then the static mechanical equilibrium equation can be written as,

$$\nabla\cdot\boldsymbol{\sigma} + \vec{F_b} = 0 \tag{10}$$

where $\vec{F_b}$ denotes the body force. We then can combine Eqs. (8)–(10) and have the poro-thermal-elastic Navier equation.

$$\nabla(\alpha P + 3\beta K\Delta T) + (\lambda + G)\nabla(\nabla\cdot\vec{u}) + G\nabla^2\vec{u} + \vec{F_b} = 0 \tag{11}$$

Taking the divergence of Eq. (11) leads to

$$\nabla^2(\alpha P + 3\beta K\Delta T) + (\lambda + 2G)\nabla^2(\nabla\cdot\vec{u}) + \nabla\cdot\vec{F_b} = 0 \tag{12}$$

The trace of the stress tensor is an invariant, and based on Eq. (8) it can be written as,

$$K\varepsilon_v = \sigma_{\text{mean}} - (\alpha P + 3\beta K\Delta T) \tag{13}$$

where σ_{mean} is the first stress invariant divided by 3, which corresponds to the uniform confining stress in laboratory experiments (Zoback, 2010); ε_v is the volumetric strain. Since the divergence of the displacement vector is the volumetric strain, we can combine Eq. (12) and Eq. (13) into,

$$\nabla\cdot\left[\nabla(\alpha P + 3\beta K\Delta T) + \frac{\lambda + 2G}{K}\nabla(\sigma_{\text{mean}} - \alpha P - 3\beta K\Delta T) + \vec{F_b}\right] = 0 \tag{14}$$

Since the reservoir is assumed to be isothermal in this study, we can simplify Eq. (14) to

$$\nabla\cdot\left[\nabla(\alpha P) + \frac{\lambda + 2G}{K}\nabla(\sigma_{\text{mean}} - \alpha P) + \vec{F_b}\right] = 0 \tag{15}$$

K, G, and λ can be expressed as the combination of Young's modulus E and Poisson's ratio ν. Finally, we have

$$\nabla\cdot\vec{\psi} = 0 \tag{16}$$

Eq. (16) represents the conservation of momentum, where $\vec{\psi}$ is the momentum flux vector. To handle different geomechanical properties in the neighboring grids n and m, the momentum flux between them can be evaluated with rock properties of two different girds respectively using the finite difference approximation, i.e., one calculated using properties and primary variables at node m, and the other using properties and primary variables at node n (Winterfeld and Wu, 2018).

$$\vec{\psi}_{m,int}\cdot\hat{n} = \frac{3(1-\nu_m)}{1+\nu_m}\frac{\sigma_m - \sigma_{nm+1/2}}{d_m} + \vec{F}_{b,m}\cdot\hat{n} - \frac{2\alpha_m(1-2\nu_m)}{1+\nu_m}\frac{P_m - P_{nm+1/2}}{d_m} \tag{17}$$

$$\vec{\psi}_{\text{int},n}\cdot\hat{n} = \frac{3(1-\nu_n)}{1+\nu_n}\frac{\sigma_{nm+1/2} - \sigma_n}{d_n} + \vec{F}_{b,n}\cdot\hat{n} - \frac{2\alpha_n(1-2\nu_n)}{1+\nu_n}\frac{P_{nm+1/2} - P_n}{d_n} \tag{18}$$

where $\hat{n}$, the normal unit vector of the interface can either be towards node n or m, but must be consistent for the same interface. The above two fluxes are identical due to the continuity assumption,

$$\vec{\psi}_{m,int}\cdot\hat{n} = \vec{\psi}_{\text{int},n}\cdot\hat{n} = \vec{\psi}_{mn}\cdot\hat{n}$$

We can then erase the mean stress at the interface $\sigma_{nm+1/2}$ by manipulating Eq. (17) and Eq. (18) and have,

$$\vec{\psi}_{mn}\cdot\hat{n} = \left[\sigma_m - \sigma_n + \frac{(1+\nu_m)d_m}{3(1-\nu_m)}\vec{F}_{b,m}\cdot\hat{n} - \frac{(1+\nu_n)d_n}{3(1-\nu_n)}\vec{F}_{b,n}\cdot\hat{n} - \frac{\frac{2(1-2\nu_m)}{3(1-\nu_m)}\alpha_m(P_m - P_{nm+1/2}) - \frac{2(1-2\nu_n)}{3(1-\nu_n)}\alpha_n(P_n - P_{nm+1/2})}{\frac{(1+\nu_m)d_m}{3(1-\nu_m)} + \frac{(1+\nu_n)d_n}{3(1-\nu_n)}}\right] \tag{19}$$

Like the mass balance equation, we could write the residual form of discretized mean stress equation as,

$$R^{t+1}_{\sigma,n} = \sum_{m\in\eta_n}\left(\vec{\psi}^{t+1}_{mn}\cdot\hat{n}\right)A^{t+1}_{nm} \tag{20}$$

The fluid flow is coupled with geomechanics by solving Eq. (20) simultaneously with mass balance equations. We can then calculate all the components in the stress tensor once the mean stress is solved by Eq. (20) (Winterfeld and Wu, 2016). As mentioned above, $Nc + 2$ governing equations are established to solve for $Nc + 2$ primary variables, which are water saturation S_w, oil phase pressure P_o, overall mole fraction Z_1, ..., Z_{Nc-1} for the components existing in both oil and gas phases and mean stress σ_{mean}.

2.2. VLE calculation with the nanopore confinement

Once the primary variables are solved by Newton's iteration, a Vapor-Liquid Equilibrium (VLE) calculation subroutine is called to calculate the saturations of gas and oil phases, as well as their mole fractions. In tight reservoirs, the sizes of pores and pore-throats in the matrix are in the scale of nanometers (Nelson, 2009; Kamruzzaman, 2015), which might lead to a substantial capillary pressure between liquid and vapor phases at equilibrium and hence affect the VLE calculation. Firincioglu et al. (2012) studied the effect of pore confinement on thermodynamic phase behaviors by including capillary pressure and van der Waals forces in the flash calculation. It is found that the contribution of surface forces is trivial compared to the capillary force on the influence of phase behaviors. Similar studies also showed that nanopore confinement could further affect other thermodynamic properties such as viscosity, density, and the minimum miscibility pressure (Teklu et al., 2014; Wang et al., 2016). Experimental studies based on nanofluidics also witnessed the deviation of the saturation pressure of hydrocarbons in nanochannels (Wang et al., 2014; Parsa et al., 2015). The influence of nanopore confinement on primary depletion has been investigated by many researchers, and generally, it is recognized as favorable in a black oil system due to suppressed bubble point (Alharthy et al., 2016). In gas condensate system, the increased dew point pressure may lead to a negative impact, but it is less pronounced as the IFT is often small between hydrocarbon liquid and vapor (Shapiro and Stenby, 2001). The main difference between the VLE calculation without confinement and the VLE calculation with confinement is the treatment of phase pressure. Instead of assuming the pressure of liquid and vapor phases as identical, the VLE with confinement would consider their difference caused by the capillary pressure,

$$f_i^L = \varphi_i^L x_i P_L = f_i^V = \varphi_i^V y_i P_V \Rightarrow K_i = \frac{y_i}{x_i} = \frac{P_L\varphi_i^L}{P_V\varphi_i^V} = \frac{P_L\varphi_i^L}{(P_L + P_c)\varphi_i^V}$$

The VLE calculation algorithm used in this study is modified from the previous work by Xiong (2015), which focused on the depletion process. And the bubble point pressure calculation subroutine is called only when the pressure of a grid is smaller than bubble point pressure P_b plus a tolerance value ΔP_{tor}, e.g. 145 psi or 1 MPa

$$P_o < P_b + \Delta P_{\text{tor}} \tag{21}$$

Then, the simulator will proceed with a standard two-phase flash. This method would work well for the primary depletion of a black-oil reservoir. However, for a gas injection case or depletion of a volatile oil or condensate gas reservoir, such criteria for phase stability would fail. In this study, instead of calculating saturation pressure which costs the same computationally as the VLE calculation, a negative flash algorithm (Whitson and Michelsen, 1989; Wang et al., 2014) is used. Limiting the liquid mole fraction L within the interval [0,1] is relaxed to $[1/(1-K_{\max}), 1/(1-K_{\min})]$ which would be more robust for gas injection. Relaxing the solution interval of L could still guarantee a physical value when calculating fugacity with Peng-Robinson EOS and estimating interfacial tension σ_{og} by Katz et al. (1943),

$$\sigma_{og}^{1/4} = \sum_{1}^{N_c} \chi_i (\rho_o x_i - \rho_g y_i) \tag{22}$$

where the parachor of a component χ_i can be estimated from experimental data (Weinaug and Katz, 1943) and the molar density ρ_o and ρ_g are calculated directly from EOS. Once the negative flash with nanopore confinement is converged, secondary variables such as L, molar composition of the liquid phase (x_1, ...,x_{Nc-1}), and molar composition of vapor phase (y_1, ...,y_{Nc-1}) need to be ensured in the physical range for the purpose of calculating the residual of mass balance equations. For example, if L is smaller than 0, then for a single-phase vapor, the molar fraction of a components in the liquid x_i, liquid phase density and saturation need to be reset as 0 and y_i should be set as z_i instead of using the results returned directly from the negative flash subroutine.

2.3. Coupling of nanopore confinement and geomechanics

The need for coupling stress and nanopore confinements arises from the fact that capillary pressure between oil and gas phase is often related to pore radius r from the Young-Laplace equation (Danesh, 1998),

$$P_c = \frac{2\sigma_{og}\cos\theta}{r(\sigma')} \tag{23}$$

where r is treated as a function of effective stress $\sigma' = \sigma_{mean} - \alpha P$. The dominant pore radius can generally be expressed as a function of stress-dependent permeability and porosity.

$$r = C_1 \left[\frac{k(\sigma')}{\phi(\sigma')}\right]^{C_2} \tag{24}$$

where C_1 is a factor based on the pore geometry. Due to the requirement of dimensional consistency (Tian et al., 2019), C_2 is often specified as 0.5. For the stress-dependent porosity, a correlation developed by McKee et al. (1988) is used in this study,

$$\phi = \phi_0 \frac{e^{-c_p \Delta\sigma'}}{1 - \phi_0 (1 - e^{-c_p \Delta\sigma'})} \tag{25}$$

For the stress-dependent permeability, an exponential model is mostly applicable based on related experimental studies (Cho et al., 2013; Tian, 2014),

$$k = k_0 e^{-C_3 \Delta\sigma'} \tag{26}$$

If C_3 is not available from experiments, McKee et al. (1988) suggested using $C_3 = 3c_p$. The coupling process exists in two levels. Firstly, geomechanics is coupled with flow when solving for primary variables. Also, the VLE calculation with nanopore confinement is coupled with stress-dependent rock properties, whose algorithm is shown in Fig. 2. The blue shaded area is where certain secondary variables mentioned above are not within the physical range, but such treatments could provide more robustness especially for considering nanopore confinement effect near the phase boundary. The unphysical value of secondary variables will be corrected accordingly once the negative flash converges. Then the corrected secondary variables will be plugged into the governing equations for the next Newton's iteration, which is vital for the mass balance equations.

3. Simulation of gas huff-n-puff

3.1. Description of the base case

The conceptual model for the base case is shown in Fig. 3, which consists of the stimulated reservoir volume (SRV) and the unstimulated rock. Within the SRV, there is a hydraulic fracture stage with four perforation clusters. The planar hydraulic fracture is modeled explicitly by logarithmically refining local grids near the hydraulic fracture face. Within a hydraulic fracture, it is assumed that the fracture tip region is unpropped therefore has a smaller width and conductivity (Cheng, 2012), and is more sensitive to the effective stress change than the propped part of a hydraulic fracture. MINC (Multiple INteracting Continua) is used to model the reactivated natural fractures in the SRV. It has been shown in previous studies (Wang and Narasimhan, 1985; Wu and Pruess, 1988) that both dual porosity and dual permeability model agree well with MINC and each of them can be treated as a special case of MINC with only two interacting continua. The unstimulated reservoir rock is also handled with MINC as a fractured medium, but with a lower permeability. Due to the symmetric nature of the conceptual model, only a fraction of the model is simulated.

Key dimensions of the model are based on the data of published studies (Gong et al., 2013; Wan et al., 2016; Phi and Schechter, 2017), which are mostly in field units. After conversion to SI units, the geometry of the base case is summarized in Table 1.

The grid system of the fractional model is shown in Fig. 4. A near wellbore simulation approach is used, i.e. fine grids are used near the perforation. Three layers are defined vertically with a total thickness of 30.48 m (100 ft), where the hydraulic fracture is assumed to be contained in the second layer and it has the same sizeas the propped fracture height in K direction as 10.97 m (36 ft). The width of the model is 27.43 m (90 ft) in I direction, which is the same as the cluster spacing. The length of the model is 198.12 m (650 ft), which is half of the horizontal well spacing. The shaded grids represent the hydraulic fracture which has a total half-length of 64.01 m (210 ft), of which 54.86 m (180 ft) is assumed to be supported by proppants. The grids close to the hydraulic fracture face in I direction and close to the fracture tip in J direction were both logarithmically refined. After the refinement, the model has 7, 12, 3 grids in I, J, K directions respectively. The active grid number for the base case is 504 because each primary grid has two subgrids, i.e., natural fracture and matrix.

In the conceptual model, there are five different porous media including propped hydraulic fractures (HF), unpropped hydraulic fractures, natural fractures (NF) in SRV, NF outside SRV and the matrix. The area surrounded by the red dash line in Fig. 4 is the SRV whose natural fracture media are assumed to be reactivated, and hence have a higher permeability than the natural fracture outside SRV. The hydraulic properties of different porous media are specified based on previous studies (Chaudhary et al., 2011; Phi and Schechter, 2017; Yu et al., 2018) and are summarized in Table 2. Since the hydraulic fracture is modeled explicitly by logarithmically refined grids, and the grid width w_{grid} containing HF as 0.61 m (2 ft) is much larger than the actual HF width w_{HF} as 3.048×10^{-4} m (0.001 ft). The grid effective permeability k_{HFeff} is scaled accordingly to maintain the same fracture conductivity as specified (CMG, 2016).

$$k_{HFeff} = \frac{k_{HF} w_{HF}}{w_{grid}} \tag{27}$$

For example, the grid effective permeability for the propped HF is 9.87×10^{-14} m^2 (100 mD), which is obtained by dividing the propped HF's conductivity 6.02×10^{-14} m^3 (200 mD-ft) with the grid width 0.61 m (2 ft). The reservoir is initially at 5.602×10^7 Pa (8125 psi) and 405.37 K (270 °F). Initial water saturation is 17% in both the matrix and fracture network.

The geomechanical properties of different porous media are estimated based on Mokhtari et al. (2014) and are summarized in Table 3. It is noted that the fracture is set as less stiff than the matrix, with a smaller Young's modulus, but higher compressibility and Biot's coefficient assuming it is more stress-dependent than the matrix. The mean stress is assumed to be 6.65×10^7 Pa (9645 psi) based on the data published by Guo et al. (2018) and the mean stress is assumed to be constant at the boundary.

The compositions of the reservoir oil are based on the published data (Yu et al., 2018), where six pseudo components are used to represent a typical black oil composition in the Eagle Ford shale as shown

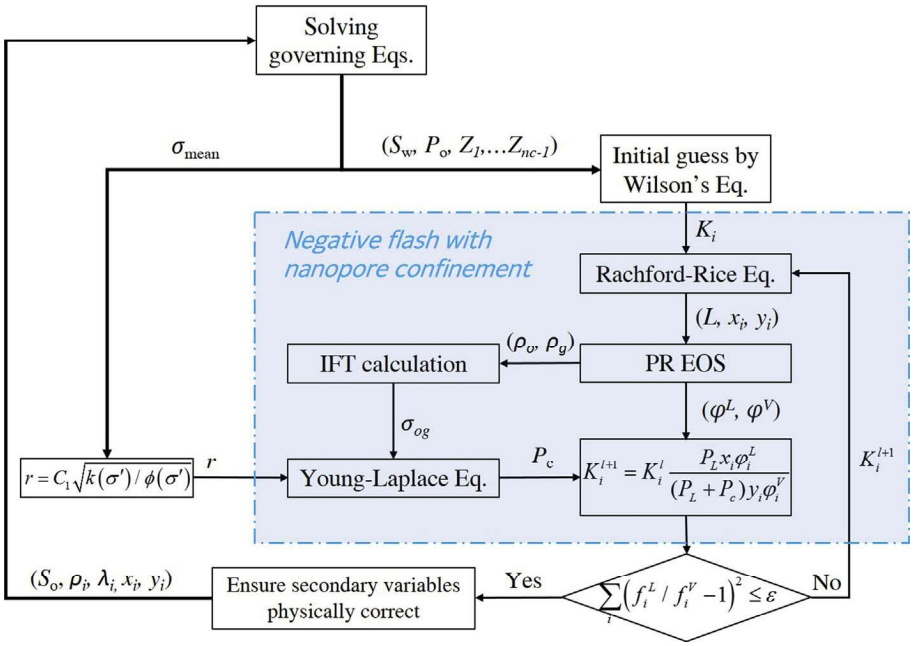

Fig. 2. Coupling of nanopore confinement and geomechanics in VLE calculation.

in Table 4. The bubble point P_b and gas-oil ratio (GOR) above P_b estimated by CMG-WinProp is 1.09×10^7 Pa (1585 psi) and 168.06 m^3/m^3 (943.6 scf/stb).

The relative permeability curves for matrix were based on the published data (Yu et al., 2018) and were smoothened by CMG before use as shown in Fig. 5.

The relative permeability curves within the fracture networks were generated and smoothened by assuming minimal residual saturation for all phases as shown in Fig. 6. The same relative permeability curves were used in all cases in this study. The critical gas saturation was set as 0.050 in the fracture network which was lower than that in the matrix as 0.127.

3.2. Model validation

The base case was built and simulated with both CMG-GEM and our in-house compositional simulator MSFLOW-COM. Since CMG-GEM neither accounts for nanopore confinement nor is fully coupled with geomechanics, the validation case built with MSFLOW-COM does not account for either effect. The well was first depleted for 720 days and was then put on a gas huff-n-puff process. The molar composition of injected gas is 91% CH_4, and 9% CO_2, assuming all C2+ components are effectively recovered in the produced gas. The gas was being injected into this single horizontal well for 150 days with a constant rate of 2.93×10^4 m^3/day (1033.6 Mscf/day), which is almost equal to the total gas produced in the previous depletion. The well was shut-in for

Table 1
Geometry of the base case for reservoir simulation.

Well geometry		Fractional model	
Perforated lateral length, m	2084.83	X, m	27.43
Stage number	19	Y, m	198.12
Clusters per stage	4	Z, m	30.48
Cluster spacing, m	27.43	Fracture half-length, m	64.01
Formation thickness, m	30.48	Fracture height, m	10.97

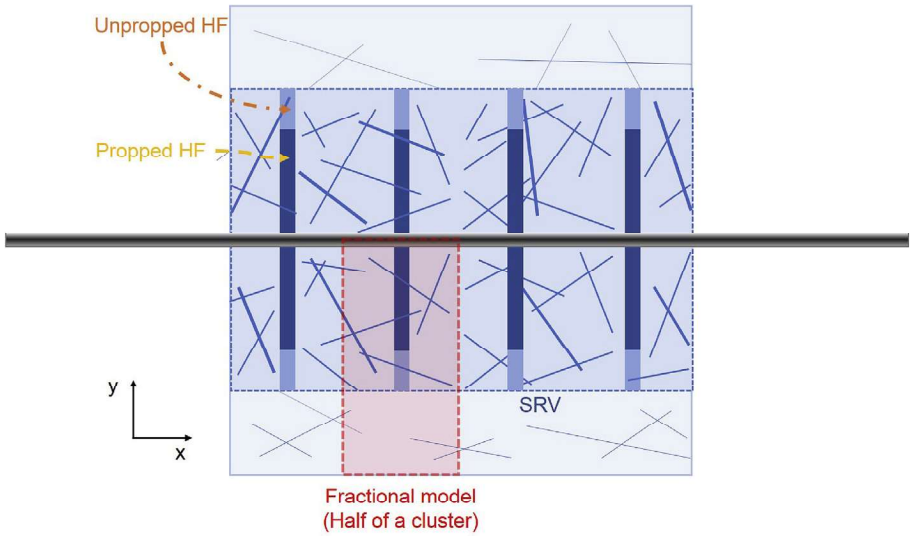

Fig. 3. Schematic of the conceptual reservoir model.

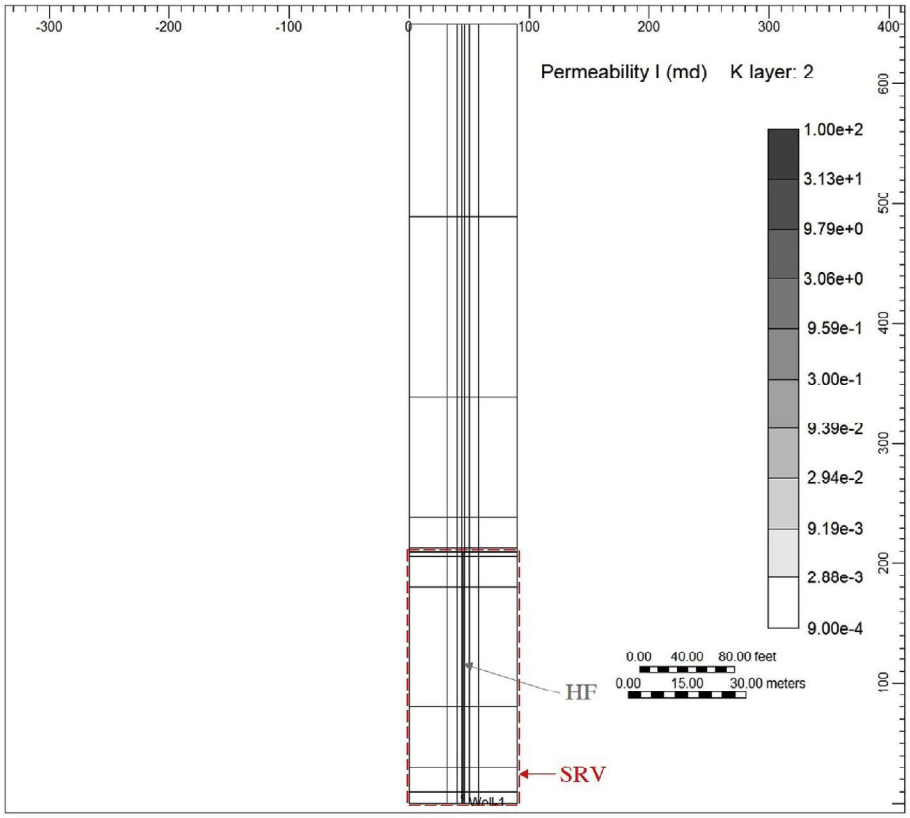

Fig. 4. The grid system in the I-J plane for the base case.

Table 2
The hydraulic properties of different porous media.

	Properties	Value	Unit
Propped HFs	Permeability	1.97×10^{-10} (2.0×10^{5})	m^2 (mD)
	Width	3.05×10^{-4} (1.0×10^{-3})	m (ft)
	Porosity	50	%
Unpropped HFs	Permeability	9.87×10^{-11} (1.0×10^{5})	m^2 (mD)
	Width	9.14×10^{-5} (3.0×10^{-4})	m (ft)
	Porosity	5	%
NFs in SRV	Permeability	8.88 E× 10^{-16} (9.0×10^{-1})	m^2 (mD)
	Spacing, m	3.048 (10)	m (ft)
	Porosity	0.12	%
NFs outside SRV	Permeability	4.4412×10^{-17} (4.5×10^{-2})	m^2 (mD)
	Spacing	3.048(10)	m (ft)
	Porosity	0.12	%
Matrix	Permeability	8.8823×10^{-19} (9.0×10^{-4})	m^2 (mD)
	Porosity	12	%

30 days after injection. Finally, the well was put on production with a constant bottom hole pressure (BHP) for another 180 days.

The daily oil rate for 1081 days was multiplied by a factor of 152 because the fractional model only represented a 1/152 fraction of the entire well. The result was then compared with CMG-GEM as shown in Fig. 7. Since the lowest BHP is 1.26×10^7 Pa (1824 psi) which is above the bubble point, the GOR calculated from MSFLOW-COM is a constant as 168.75 m^3/m^3 (947.5 scf/stb) which is close to CMG-GEM's value as 168.06 m^3/m^3 (943.6 scf/stb). For the pressure and oil saturation at the fracture grid containing the wellbore, there was no need to scale and the results were also compared with CMG-GEM and shown in Fig. 8. MSFLOW-COM could obtain a very close result compared with CMG-GEM for both the depletion and gas huff-n-puff stage, which verified our compositional model as well as the correctness of the numerical approach to solve the model. Besides, MSFLOW-COM has been verified

Table 3
The geomechanical properties of different porous media.

Rock types	Properties	Value	Unit
Propped HFs	Compressibility	1.09×10^{-9} (7.5×10^{-6})	Pa^{-1} (psi^{-1})
	Young's modulus	6.89×10^{9} (1.0×10^{6})	Pa (psi)
	Poisson's ratio	0.26	
	Biot's coefficient	0.9	
Unpropped HFs	Compressibility	1.09×10^{-9} (7.5×10^{-6})	Pa^{-1} (psi^{-1})
	Young's modulus	6.89×10^{9} (1.0×10^{6})	Pa (psi)
	Poisson's ratio	0.26	
	Biot's coefficient	0.8	
NFs in SRV	Compressibility	1.09×10^{-9} (7.5×10^{-6})	Pa^{-1} (psi^{-1})
	Young's modulus	1.03×10^{10} (1.5×10^{6})	Pa (psi)
	Poisson's ratio	0.26	
	Biot's coefficient	0.75	
NFs outside SRV	Compressibility	1.09×10^{-9} (7.5×10^{-6})	Pa^{-1} (psi^{-1})
	Young's modulus	1.03×10^{10} (1.5×10^{6})	Pa (psi)
	Poisson's ratio	0.26	
	Biot's coefficient	0.75	
Matrix	Compressibility	7.25×10^{-10} (5.0×10^{-6})	Pa^{-1} (psi^{-1})
	Young's modulus	1.38×10^{10} (2.0×10^{6})	Pa (psi)
	Poisson's ratio	0.26	
	Biot's coefficient	0.7	

Table 4
Properties of a typical Eagle Ford black oil sample.

Component	Composition	P_c, MPa	T_c, K	Acentric factor	MW, g/mol
CO_2	0.012	7.376	304.20	0.2250	44.01
N_2	0.002	3.394	126.20	0.0400	28.01
CH_4	0.115	4.600	190.60	0.0080	16.04
C2-5	0.264	3.698	274.74	0.1723	52.02
C6–C10	0.381	2.541	438.68	0.2839	103.01
C11+	0.226	1.778	740.29	0.6716	267.15

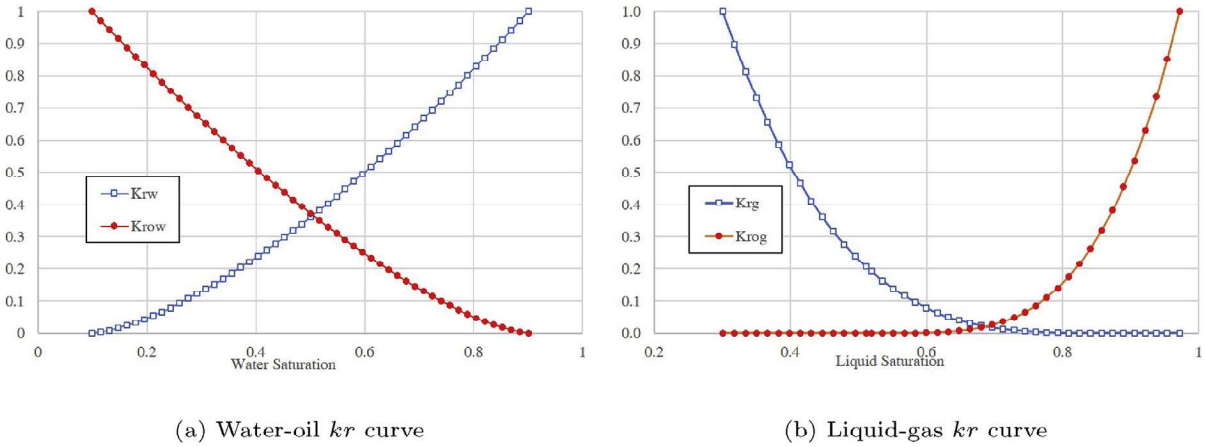

Fig. 5. The relative permeability curve for the matrix.

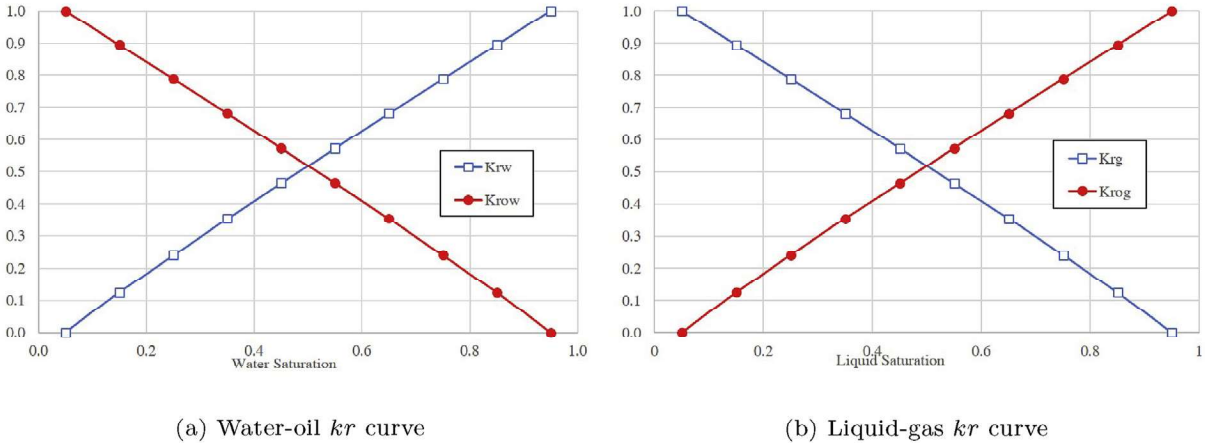

Fig. 6. The relative permeability curve for the fracture network.

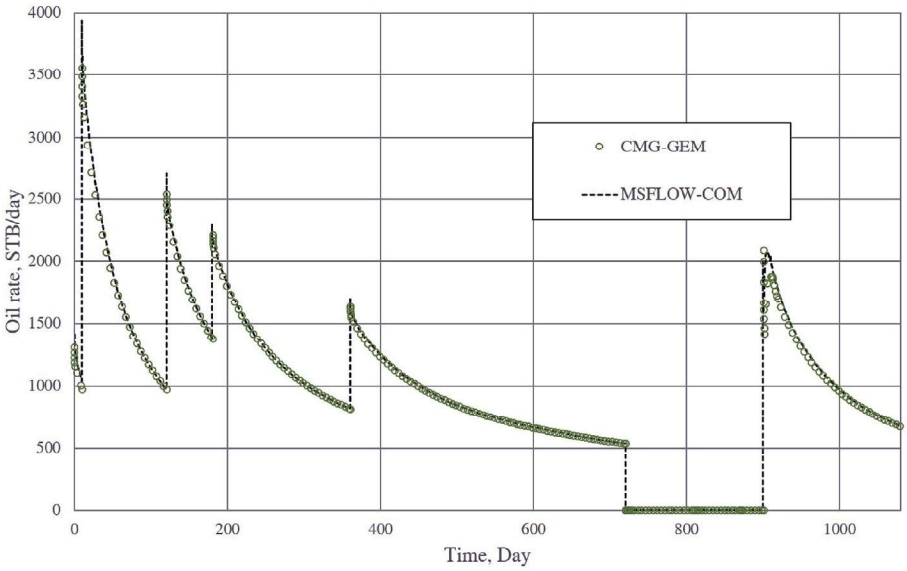

Fig. 7. Comparison of the daily oil rate between CMG-GEM and MSFLOW-COM.

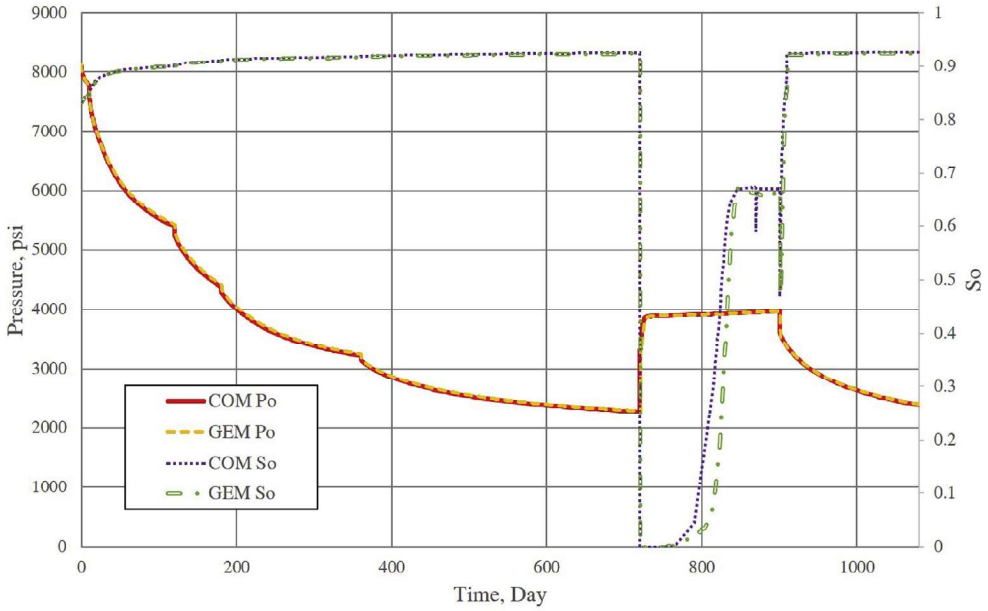

Fig. 8. Comparison of oil saturation and pressure at the grid containing the perforation.

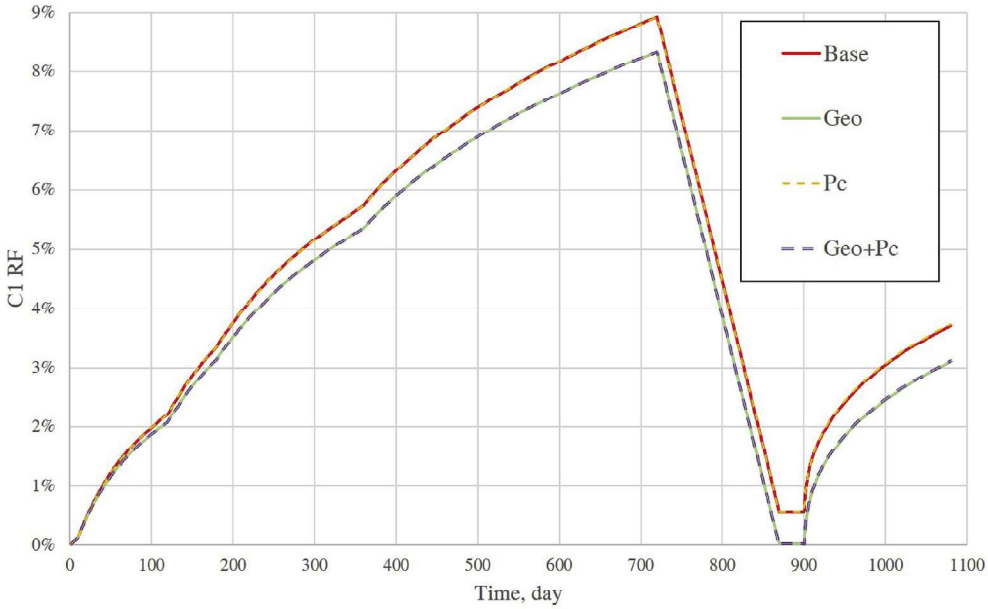

Fig. 9. Comparison of the RF of CH_4 among Case 1-4.

against experimental data, analytical solutions in the previous work by Xiong (2015).

4. Results and discussions

Besides the base case (Case 1, Base), several other cases were built and run with MSFLOW-COM. Case 2 (Geo) included the geomechanical effects i.e. simultaneously solving the stress equation and considering stress-dependent porosity, permeability, and rock volume. Case 3 (Pc) accounted for the nanopore confinement effect in the VLE module but not geomechanical effects. Case 4 (Geo + Pc) coupled the nanopore confinement and geomechanics. All cases in this study did not account for molecular diffusion although it is available as an option in MSFLOW-COM. The recovery factors for CH_4 and C2-5 component were plotted in Fig. 9 and Fig. 10. Because CH_4 was the major component of the injected gas, its RF would decline during the huff-n-puff.

By comparing the base Case 1 (Base) versus Case 3 (Pc) or Case 2 (Geo) versus Case 4 (Geo + Pc), it seems nanopore confinement has a very limited impact on the RF during both depletion and the first cycle of gas huff-n-puff. This is because the initial reservoir pressure as 5.602×10^7 Pa (8125 psi) is much higher than bubble point pressure as 1.09×10^7 Pa (1585 psi) and during depletion, the BHP as 1.26×10^7(1824 psi) is maintained well above the bubble point pressure. Essentially, this is because when the reservoir pressure is much higher than the saturation pressure, VLE calculation will lead to only one phase, and finally yield an interfacial tension value of zero. But once the overall fluid composition gets close to phase boundary or the shadow region boundary defined by Michelsen and Mollerup (2007), the VLE iteration will give two phases i.e. one liquid-like, and the other vapor-like. Then, interfacial tension will no longer be evaluated as zero and nanopore confinement will start to affect phase behaviors, which is the case for reservoirs near the saturation pressure or with more huff-n-

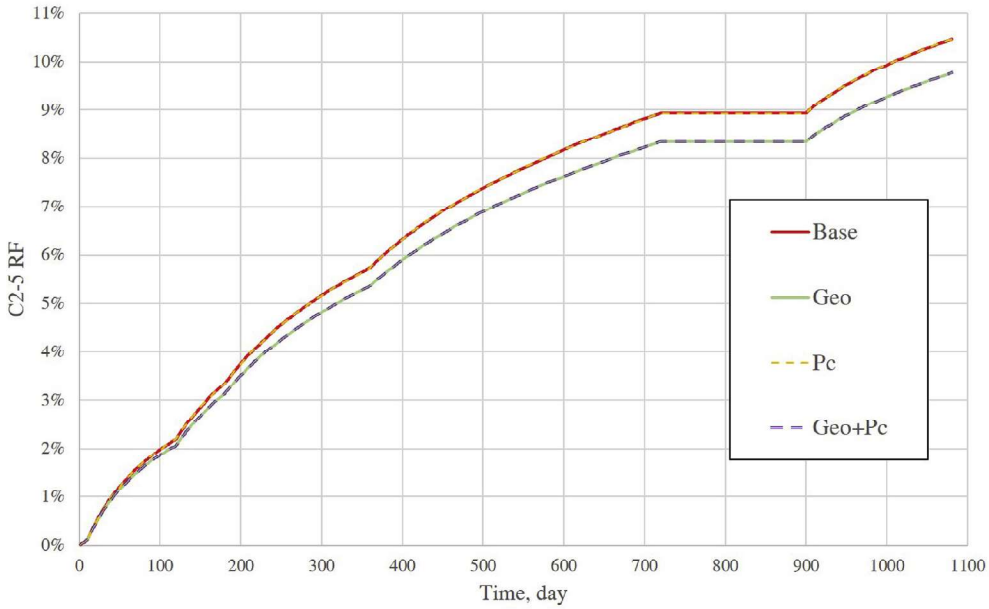

Fig. 10. Comparison of the RF of C2-5 among Case 1-4.

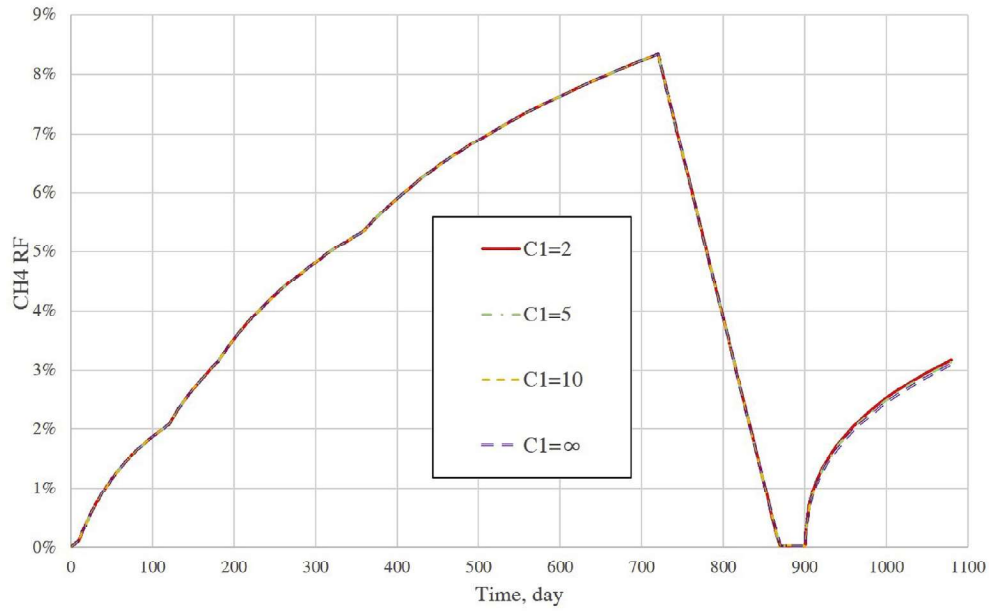

Fig. 11. The RF of CH_4 with different pore sizes.

puff cycles. At the convergence of flash calculation, even if pressure is found to be still above saturation pressure and the vapor-like phase is discarded as a trivial solution, the phase behavior has been affected by nanopore confinement within the iterations of VLE calculation.

Coupling the geomechanics with flow would appreciably affect the RF for both CH_4 and C2-5 by comparing the base Case 1 (Base) and Case 2 (Geo). This is because the stress field and essentially the effective stress will affect porosity, rock bulk volume and permeability. And we will show a detailed sensitivity analysis of this issue later.

In Case 5 and 6, different values of C_1 in Eq. (24) were specified ($C_1 = 2, 5$), which essentially represents different dominant pore sizes and their capillary effects on VLE calculation. C_1 was chosen as 10 in the base case, which leads to an effective matrix pore radius as 27 nm. The comparison among Case 2 (without capillary effect, $C_1 = \infty$, $r = \infty$), Case 3 ($C_1 = 10$, $r = 27$ nm), Case 5 ($C_1 = 2$, $r = 5.4$ nm) and Case 6 ($C_1 = 5$, $r = 13.5$ nm) indicates that the nanopore confinement has very limited influence on a component's recovery factor as shown in Fig. 11 and Fig. 12. The main reason is that the reservoir pressure was maintained above the bubble point and the overall composition in the matrix is far away from the shadow region boundary. In fractures, though vapor and liquid phase may coexist in equilibrium, the effect of nanopore confinement is still negligible due to a very large dominant pore size (>100 nm).

On the basis of Case 4, Case 7 and 8 investigated the effect of fracture Biot's coefficient on RF. A higher Biot's coefficient means that pore fluids contribute more to counter the confining stress (e.g. 1 for soil). Fracture, which is less compacted and filled with less rock grains than matrix, is often characterized with a higher α. Walsh (1981) concluded that the Biot's coefficient for joints with polished surface is 0.9 and Biot's coefficient is 0.56 for rocks with tensile fractures. Abass et al. (2009) measured the Biot's coefficient for a tight sandstone as 0.35. After artificially creating a tensile fracture, the Biot's coefficient

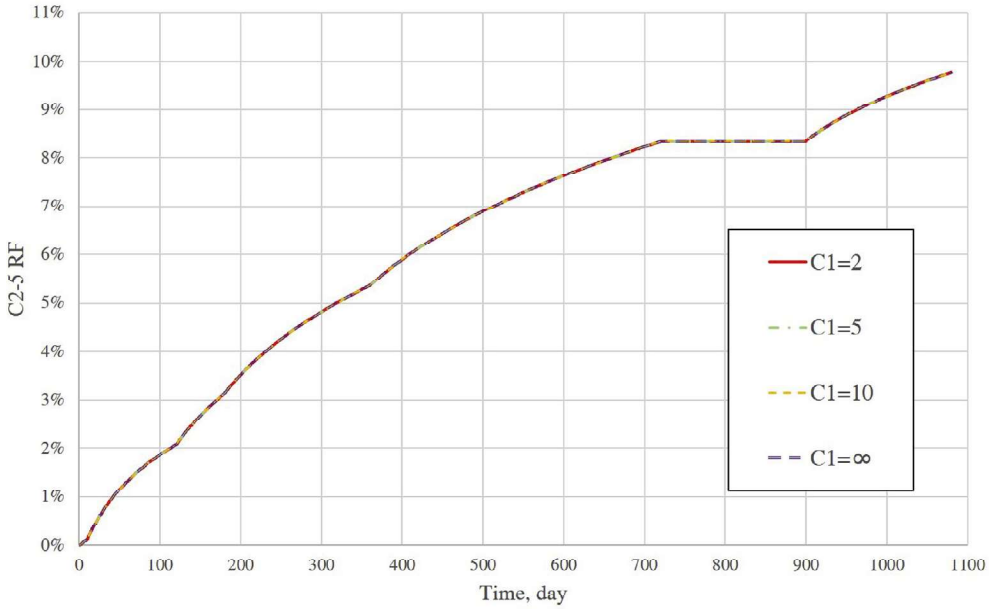

Fig. 12. The RF of C2-5 with different pore sizes.

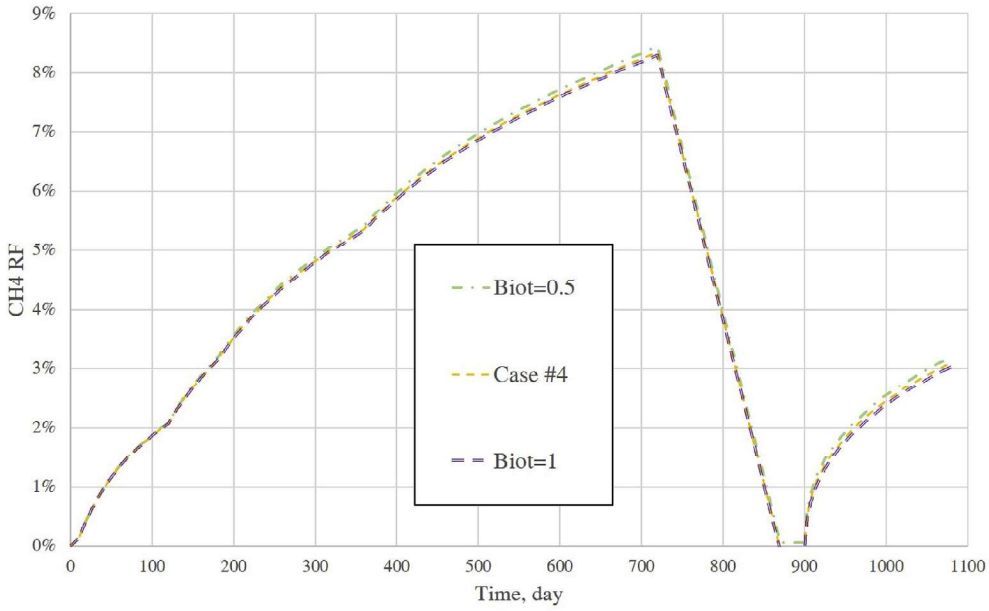

Fig. 13. The RF of CH_4 with different Biot's coefficients for fractures.

was measured as 0.95. Cui and Abass, 2016 applied the same approach to Niobrara shale, and found a Biot's coefficient of 0.8 for matrix dominant core and 1 for fractured dominated core. Hence, different Biot's coefficients for fracture are investigated while maintaining the same α for matrix. Case 7 assumed that all fracture media had the same Biot's coefficient as 0.5 and Case 8 assumed that all fracture media had the same Biot's coefficient as 1. Case 4 specified different Biot's coefficient for different media as shown in Table 3 which could be treated as an intermediate scenario between Case 7 and 8. With a larger Biot's coefficient, the change in pore pressure should have a larger impact on the effective stress. With increasing Biot's coefficient, the RF for both CH_4 and C2-5 were reduced due to decreased permeability in the fracture network as shown in Fig. 13 and Fig. 14.

In Case 9, 10 and 11, different values of Biot's coefficient (α = 0.1, 0.4, 1) were specified for the matrix. As shown in Fig. 15 and Fig. 16, a higher Biot's coefficient led to a higher recovery factor for both CH_4 and C2-5 component which is opposite to the cases in the fracture media. This is because the effect of permeability reduction due to increased effective stress was compensated by a more efficient reduction of pore volume due to compaction, i.e. enhanced rock compaction drive. Under this scenario, the overall geomechanical effect is beneficial rather than detrimental to the recovery factor. For the gas injection stage, since the injection rate was set as a constant, its effect was minimal. However, since less gas was produced in the primary depletion with decreasing Biot's coefficient of the matrix, the RF of CH_4 might become negative as the injected gas volume was slightly higher than the produced volume.

We have so far discussed the effect of coupled geomechanics and nanopore confinement in the depletion and the first cycle of gas huff-n-puff. Below, several representative cases were extended to 3600 days with an additional seven huff-n-puff cycles to study their long-term impacts. Case 12 had the same input as Case 2 but extended cycles. Case

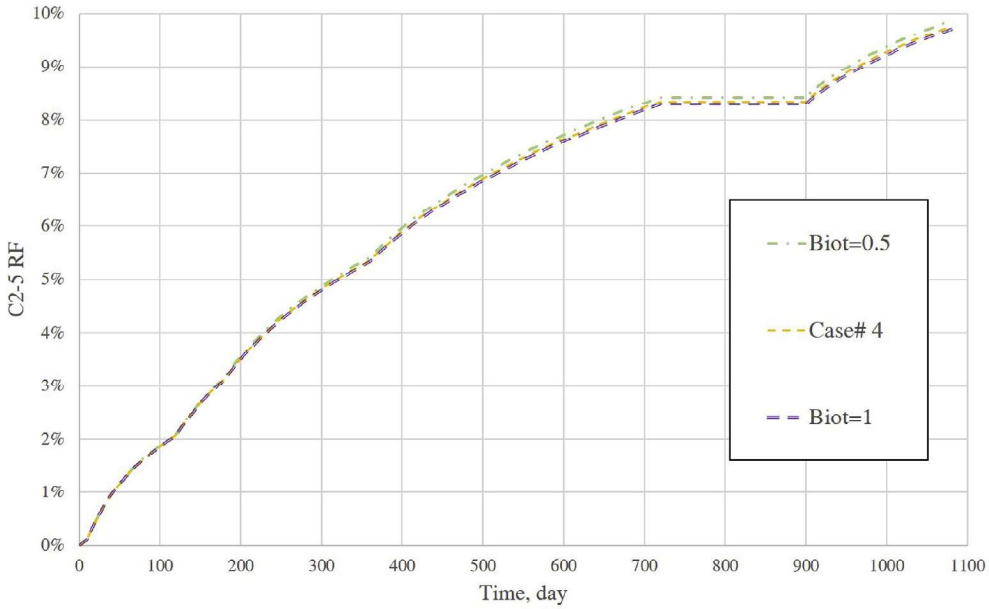

Fig. 14. The RF of C2-5 with different Biot's coefficients for fractures.

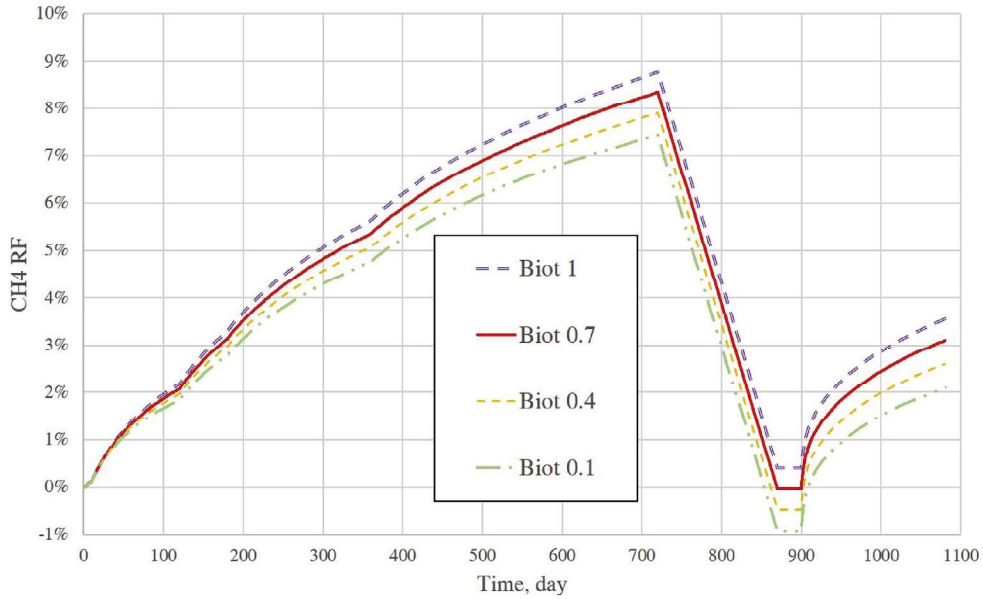

Fig. 15. The RF of CH_4 with different Biot's coefficients for the matrix.

13 was the same as Case 12 except that the gas injection stage was replaced by a shut-in. Both case 12 and 13 accounted for geomechanics but not nanopore confinement or molecular diffusion. The RF of CH_4 and CO_2 were not shown because they were the primary components of injected gas.

As shown in Fig. 17, each phase had a very similar recovery factor for the primary depletion, this is because the matrix in the reservoir was still above the bubble point. For the cyclic gas injection case, the RF was higher than the primary depletion for every component except CH_4 and CO_2. For the first cycle, each component had a similar RF. In the 2nd-6th cycle, the heavier the component, the higher the RF. After 6 cycles, there was a crossover point around the 3080th day, where the heavier component started to have a lower RF than the lighter component. In the end, the recovery factor of a lighter component was higher than a heavier component. One possible reason behind this counter-intuitive phenomenon might be that the injected dry gas would first enter the matrix near the fracture network and the equilibrium vapor phase would become richer with intermediate components (C2-5 and C6-10), but it would be further pushed away from the hydraulic fracture. However, when production resumed, due to the existence of critical gas saturation in the matrix, this vapor phase enriched with the intermediates would find it difficult to re-enter the fracture network. The mixing process is like a vaporizing gas drive but with a different flow direction. In a vaporizing gas drive, the injected gas will push the enriched vapor phase towards a producer, but gas injected during huff-n-puff will push the enriched vapor phase away from the hydraulic fracture, which acts like a de facto well. The gas in the matrix will not be able to flow towards fractures until its saturation in the matrix exceeds this critical gas saturation. As the gas phase becomes more mobile than the liquid, more lighter component will be produced. Finally, the RF of a lighter component will surpass the RF of a heavier component, which explains the crossover point in Fig. 17.

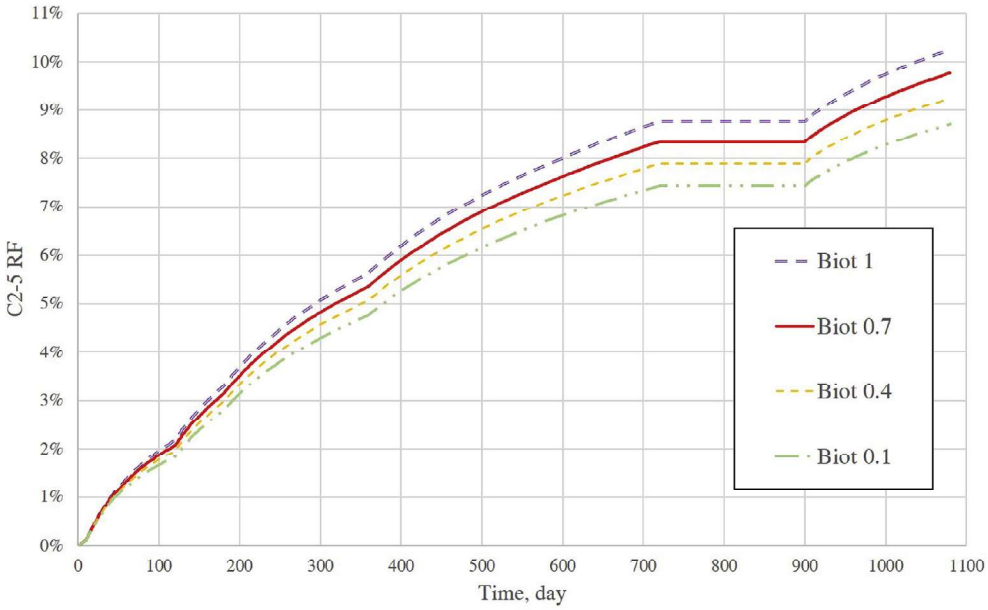

Fig. 16. The RF of C2-5 with different Biot's coefficients for the matrix.

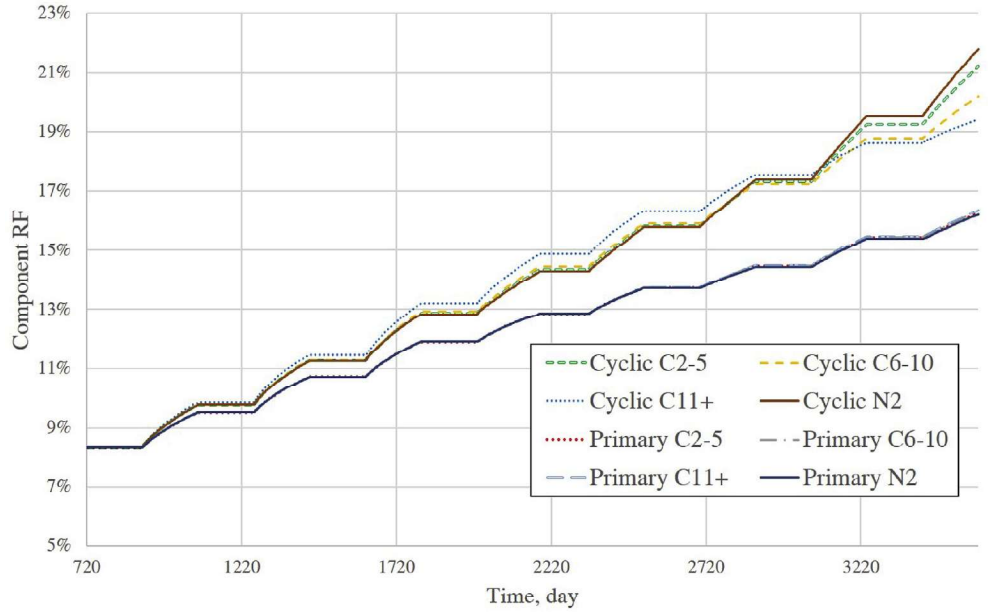

Fig. 17. Comparison of RF between depletion and gas huff-n-puff after 10 years.

Such a phenomenon is controlled mainly by the critical gas saturation of the matrix together with the upstream weighting scheme, where the fracture relative permeability controls the gas injection process and the matrix relative permeability controls the production process. Quite often, the critical gas saturation in fracture was specified as a small value making such phenomenon more significant. In Case 14, by lowering the critical gas saturation of the matrix from 0.127 to 0.05, the crossover point appeared early around 2360th day, 720 days ahead of Case 12 as shown in Fig. 18. Juanes et al. (2006) modeled the gas trapping phenomenon in CO_2 sequestration by using the concept of relative permeability hysteresis. Here we captured a similar gas trapping phenomenon by implementing different relative permeability curves based on the direction of flow , that is using fracture relative permeability curve for flows from fracture to matrix and matrix relative permeability curve for flows from matrix to fracture.

Case 15 considered coupled nanopore confinement and geomechanics while Case 12 only accounted for the geomechanics. As shown in Fig. 19, considering the effect of nanopore confinement will slightly delay the crossover point to the 3120th day. However, before the crossover point and starting from the 2700th day, the difference in RF between Case 12 and Case 15 becomes appreciable especially for N_2. The nanopore confinement lowers the RF of a lighter component, and slightly increases the RF of a heavier component. This is mainly because nanopore confinement alters the phase composition at equilibrium, i.e. making the trapped gas phase richer with light and intermediate components and the mobile oil phase leaner with them as mentioned in an earlier study by Wang et al. (2016). More light and intermediate components would be trapped in the matrix's gas phase, which would hence lower its component RF before the crossover point. In the end, light component's recovery factor would surpass the heavier component's due to higher gas mobility compared to that of the oil phase rich with C11+. Still, the above mentioned gas trapping together with

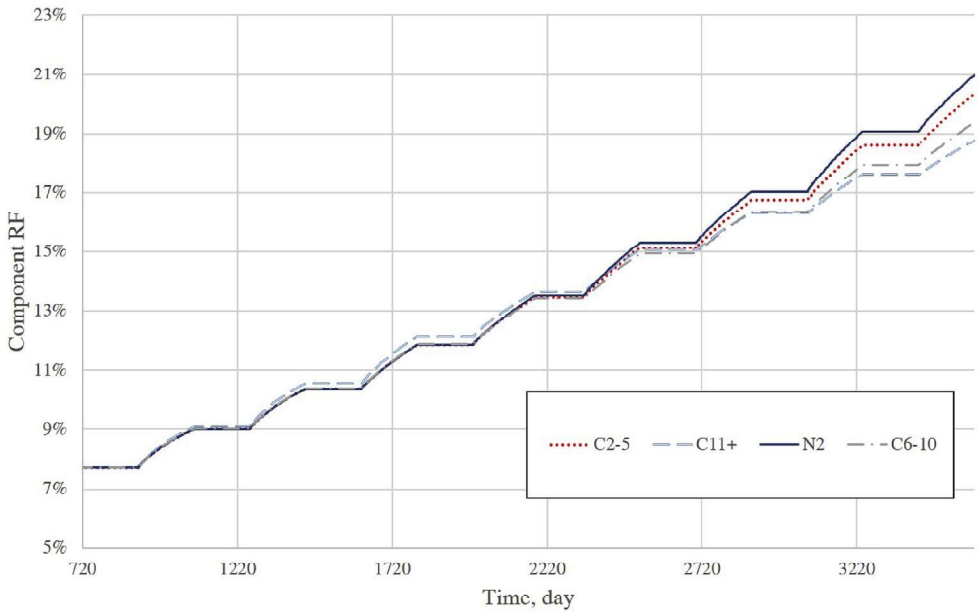

Fig. 18. RF of gas huff-n-puff with a reduced critical gas saturation in the matrix.

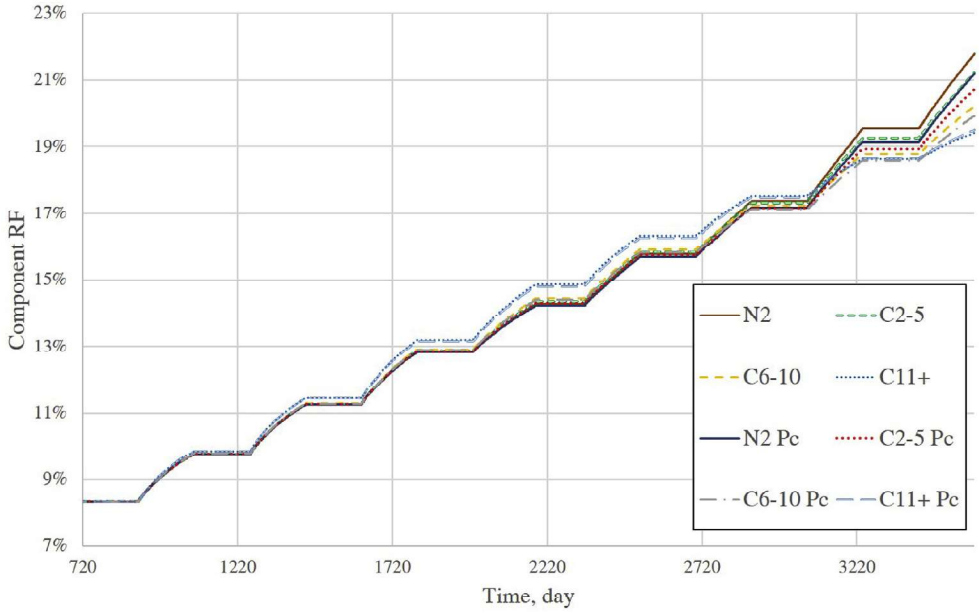

Fig. 19. RF of gas huff-n-puff with nanopore confinement after 10 years.

nanopore confinement will affect the component RF after 10 years. For a light component (N_2) or intermediate component (C2-5, C6-10), its RF under nanopore confinement would be lower than that without nanopore confinement. For a heavy component (C11+), the RF with nanopore confinement is slightly higher than that without nanopore confinement.

5. Conclusions

This study presents a multiphase multicomponent model, which is of practical use for accurately modeling primary depletion as well as gas injection processes in fractured unconventional oil reservoirs. The associated simulator was first validated against a commercial compositional simulator (CMG-GEM). Then, it was applied to study the coupled geomechanics and nanopore confinement in the primary depletion and the subsequent gas huff-n-puff in a well located in the black-oil region of Eagle Ford play.

If the reservoir pressure is much higher than the bubble point pressure, nanopore confinement will have a very limited impact on the recovery factor for both the depletion and the first few cycles of gas huff-n-puff.

Geomechanics is a very important factor in production. For the fracture network, a higher Biot's coefficient in the fracture would lead to a larger effective stress change, causing a larger reduction of fracture permeability hence a lower recovery. However, in the matrix, a higher Biot's coefficient would favor the recovery as the enhanced rock compaction drive would offset the permeability reduction.

Gas huff-n-puff would improve the component recovery factor compared with primary depletion. A heavier component would initially have a higher RF than a lighter component during the first few cycles of huff-n-puff, but its RF would be gradually outpaced by a lighter component after a crossover point. This crossover point is controlled by the

critical gas saturation of the matrix.

Lastly, considering nanopore confinement in the simulation will slightly delay the above-mentioned crossover point. Nanopore confinement will also reduce the RF of light components but increase the RF of heavy components after huff-n-puff.

Acknowledgments

The authors would like to thank Energi Simulation (formerly Foundation CMG) to support this study. Financial support from China National Petroleum Corporation under Project 2017D-5009-01, "New Technology for Effective Development and Evaluation of Ultra-low Permeability Reservoirs" is also acknowledged.

Nomenclature

α	Biot's coefficient
β	linear thermal expansion coefficient, K^{-1}
σ	stress tensor, Pa
ε	strain tensor
χ_i	parachor of a component i, $N^{1/4}$ $m^{-1/4}$
η_n	set of grids that are connected with grid n
γ_{nm}	transmissibility between two connected grids n and m, m^3
λ_j	mobility of a phase j ($j = o, g, w$), Pa^{-1} s^{-1}
λ	Lame's first parameter, Pa
ν	Poisson's ratio
φ_i^j	fugacity coefficient of component i in phase j
Φ_{jn}	flow potential of a phase j ($j = o, g, w$) at grid n, Pa
ϕ	rock porosity
ϕ_0	initial rock porosity
ρ_j	molar density of a phase j ($j = o, g, w$), mol m^{-3}
σ'	effective stress, Pa
σ_{mean}	mean stress, Pa
σ_{og}	interfacial tension between oil and gas phase, N m^{-1}
θ	contact angle
ε_v	volumetric strain
$\overrightarrow{\psi}$	momentum flux vector, N m^{-3}
$\overrightarrow{F_b}$	body force per unit volume, N m^{-3}
$\overrightarrow{u}$	rock displacement vector, m
A_{nm}	interface area between connected grid n and m, m^2
c_p	rock compressibility, Pa^{-1}
$D_{\text{eff},i}$	effective diffusion coefficient of a component i in the gas phase, m^2 s^{-1}
d_n	distance from the center of grid n to the interface, m
G	shear modulus, Pa
K_i	vapor-liquid equilibrium ratio of component i
K	bulk modulus, Pa
k_0	initial rock permeability, m^2
$k_{nm+1/2}$	harmonic averaged permeability between grid n and m, m^2
P_b	bubble point pressure, Pa
P_c	capillary pressure between oil and gas phase, Pa
P_j	pressure of a phase j ($j = o, g, w$), Pa
P_n	pore pressure at grid n, Pa
q_i	sink/source term of a component i ($i = 1, ..., Nc + 1$), mol m^{-3} s^{-1}
S_j	saturation of a phase j ($j = o, g, w$)
S_n	surface area of a grid block n, m^2
t	time, s
V_n	bulk volume of a grid block n, m^3
x_i	mole fraction of a component i in the oil phase ($i = 1, ..., Nc$)
y_i	mole fraction of a component i in the gas phase ($i = 1, ..., Nc$)
Z_i	overall mole fraction of a component i ($i = 1, ..., Nc$)
ΔT	temperature change, K
$\overrightarrow{v_j}$	volumetric flow rate of a phase j ($j = o, g, w$), m s^{-1}

References

Abass, H.H., Al-Tahini, A.M., Abousleiman, Y., Khan, M.R., et al., 2009. New technique to determine biot coefficient for stress-sensitive dual-porosity reservoirs. In: SPE Annual Technical Conference and Exhibition. Society of Petroleum Engineers.

Alharthy, N.S., Teklu, T.W.W., Nguyen, T.N., Kazemi, H., Graves, R.M., 2016. Nanopore compositional modeling in unconventional shale reservoirs. SPE Reserv. Eval. Eng. 19, 415–428.

CMG, 2016. Gem User's Guide. Computer Modeling Group Ltd., Calgary, Canada.

Chaudhary, A.S., Ehlig-Economides, C.A., Wattenbarger, R.A., 2011. Shale oil production performance from a stimulated reservoir volume. In: SPE Annual Technical Conference and Exhibition. Society of Petroleum Engineers.

Chen, C., Balhoff, M.T., Mohanty, K.K., 2014. Effect of reservoir heterogeneity on primary recovery and CO2 huff'n'puff recovery in shale-oil reservoirs. SPE Reserv. Eval. Eng. 17, 404–413.

Cheng, Y., 2012. Impacts of the number of perforation clusters and cluster spacing on production performance of horizontal shale-gas wells. SPE Reserv. Eval. Eng. 15, 31–40.

Cho, Y., Ozkan, E., Apaydin, O.G., 2013. Pressure-dependent natural-fracture permeability in shale and its effect on shale-gas well production. SPE Reserv. Eval. Eng. 16, 216–228.

Cui, Q., Abass, H., 2016. Experimental study of permeability decline in tight formations during long-term depletion. In: SPE Low Perm Symposium. Society of Petroleum Engineers.

Danesh, A., 1998. PVT and Phase Behaviour of Petroleum Reservoir Fluids, vol. 47 Elsevier.

EIA, 2019. Annual Energy Outlook 2019: with Projections to 2050. Technical Report. U.S. Energy Information Administration.

Firincioglu, T., Ozkan, E., Ozgen, C., 2012. Thermodynamics of multiphase flow in unconventional liquids-rich reservoirs. In: SPE Annual Technical Conference and Exhibition. Society of Petroleum Engineers.

Gamadi, T.D., Elldakli, F., Sheng, J., 2014. Compositional simulation evaluation of EOR potential in shale oil reservoirs by cyclic natural gas injection. In: Unconventional Resources Technology Conference, Unconventional Resources Technology Conference.

Gong, X., Tian, Y., McVay, D.A., Ayers, W.B., Lee, J., 2013. Assessment of Eagle Ford shale oil and gas resources. In: SPE Unconventional Resources Conference Canada. Society of Petroleum Engineers.

Guo, X., Wu, K., Killough, J., 2018. Investigation of production-induced stress changes for infill-well stimulation in Eagle Ford shale. SPE J. 23 (4), 1372–1388. https://doi.org/10.2118/189974-PA.

Hawthorne, S.B., Gorecki, C.D., Sorensen, J.A., Steadman, E.N., Harju, J.A., Melzer, S., 2013. Hydrocarbon mobilization mechanisms from upper, middle, and lower Bakken reservoir rocks exposed to CO2. In: SPE Unconventional Resources Conference Canada. Society of Petroleum Engineers.

Hoffman, B.T., Evans, J.G., 2016. Improved oil recovery IOR pilot projects in the Bakken formation. In: SPE Low Perm Symposium. Society of Petroleum Engineers.

Hoffman, B.T., Sonnenberg, S., Kazemi, H., Cui, Q., 2014. The benefits of reinjecting instead of flaring produced gas in unconventional oil reservoirs. In: Unconventional Resources Technology Conference, Unconventional Resources Technology Conference.

Juanes, R., Spiteri, E., Orr Jr., F., Blunt, M., 2006. Impact of relative permeability hysteresis on geological CO2 storage. Water Resour. Res. 42.

Kamruzzaman, A., 2015. Petrophysical rock typing of unconventional shale plays: a case study for the Niobrara formation of the Denver-Julesburg (DJ) Basin. Master's thesis. Colorado School of Mines.

Katz, D., Monroe, R., Trainer, R., 1943. Surface tension of crude oils containing dissolved gases. Pet. Tech. 6, 1–10.

Kurtoglu, B., Sorensen, J.A., Braunberger, J., Smith, S., Kazemi, H., 2013. Geologic characterization of a Bakken reservoir for potential CO2 EOR. In: Unconventional Resources Technology Conference, Unconventional Resources Technology Conference.

McKee, C.R., Bumb, A.C., Koenig, R.A., 1988. Stress-dependent permeability and porosity of coal and other geologic formations. SPE Form. Eval. 3, 81–91.

Michelsen, M.L., Mollerup, J., 2007. Thermodynamics Models: Fundamendals and Computational Aspects.

Mokhtari, M., Honarpour, M.M.M., Tutuncu, A.N., Boitnott, G.N., 2014. Acoustical and geomechanical characterization of Eagle Ford shale-anisotropy, heterogeneity and measurement scale. In: SPE Annual Technical Conference and Exhibition. Society of Petroleum Engineers.

Nelson, P.H., 2009. Pore-throat sizes in sandstones, tight sandstones, and shales. AAPG Bull. 93, 329–340.

Parsa, E., Yin, X., Ozkan, E., 2015. Direct observation of the impact of nanopore confinement on petroleum gas condensation. In: SPE Annual Technical Conference and Exhibition. Society of Petroleum Engineers.

Peng, X., Zeng, F., Du, Z., Yang, H., 2017. Experimental study on pressure control strategies for improving waterflooding potentials in a heavy oil-methane system. J. Pet. Sci. Eng. 149, 126–137.

Phi, T., Schechter, D., 2017. CO2 EOR simulation in unconventional liquid reservoirs: an Eagle Ford case study. In: SPE Unconventional Resources Conference. Society of Petroleum Engineers.

Pruess, K., 1991. TOUGH2-a general-purpose numerical simulator for multiphase fluid and heat flow. Lawrence Berkeley Lab, CA, United States.

Qiao, C., 2015. General purpose compositional simulation for multiphase reactive flow with a fast linear solver. Ph.D. thesis. The Pennsylvania State University.

Sanchez-Rivera, D., Mohanty, K., Balhoff, M., 2015. Reservoir simulation and optimization of huff-and-puff operations in the Bakken shale. Fuel 147, 82–94.
Shapiro, A.A., Stenby, E.H., 2001. Thermodynamics of the multicomponent vapor–liquid equilibrium under capillary pressure difference. Fluid Phase Equilib. 178, 17–32.
Sheng, J.J., 2015. Enhanced oil recovery in shale reservoirs by gas injection. J. Nat. Gas Sci. Eng. 22, 252–259.
Sheng, J.J., Chen, K., 2014. Evaluation of the EOR potential of gas and water injection in shale oil reservoirs. J. Unconv. Gas Oil Resour. 5, 1–9.
Teklu, T.W., Alharthy, N., Kazemi, H., Yin, X., Graves, R.M., AlSumaiti, A.M., 2014. Phase behavior and minimum miscibility pressure in nanopores. SPE Reserv. Eval. Eng. 17, 396–403.
Tian, Y., 2014. Experimental study on stress sensitivity of naturally fractured reservoirs. In: SPE Annual Technical Conference and Exhibition. Society of Petroleum Engineers.
Tian, Y., Yu, X., Li, J., Neeves, K.B., Yin, X., Wu, Y.S., 2019. Scaling law for slip flow of gases in nanoporous media from nanofluidics, rocks, and pore-scale simulations. Fuel 236, 1065–1077.
Uzun, I., Eker, E., Kazemi, H., Stoltz, R., 2018. An efficient compositional model for unconventional reservoirs: Eagle Ford formation case study. In: SPE Western Regional Meeting. Society of Petroleum Engineers.
Walsh, J., 1981. Effect of pore pressure and confining pressure on fracture permeability. Int. J. Rock Mech. Min. Sci. Geomech. Abstr. 18, 429–435.
Wan, T., Sheng, J., Soliman, M.Y., Zhang, Y., 2016. Effect of fracture characteristics on behavior of fractured shale-oil reservoirs by cyclic gas injection. SPE Reserv. Eval. Eng. 19, 350–355.
Wang, J., Narasimhan, T.N., 1985. Hydrologic mechanisms governing fluid flow in a partially saturated, fractured, porous medium. Water Resour. Res. 21, 1861–1874.
Wang, L., Parsa, E., Gao, Y., Ok, J.T., Neeves, K., Yin, X., Ozkan, E., 2014. Experimental study and modeling of the effect of nanoconfinement on hydrocarbon phase behavior in unconventional reservoirs. In: SPE Western North American and Rocky Mountain Joint Meeting. Society of Petroleum Engineers.
Wang, L., Yin, X., Neeves, K.B., Ozkan, E., 2016. Effect of pore-size distribution on phase transition of hydrocarbon mixtures in nanoporous media. SPE J. 21 (6), 1981–1995.
Wang, L., Tian, Y., Yu, X., Wang, C., Yao, B., Wang, S., Winterfeld, P.H., Wang, X., Yang, Z., Wang, Y., 2017. Advances in improved/enhanced oil recovery technologies for tight and shale reservoirs. Fuel 210, 425–445.
Weinaug, C.F., Katz, D.L., 1943. Surface tensions of methane-propane mixtures. Ind. Eng. Chem. 35, 239–246.
Whitson, C.H., Michelsen, M.L., 1989. The negative flash. Fluid Phase Equilib. 53, 51–71.
Winterfeld, P.H., Wu, Y.S., 2016. Simulation of coupled thermal/hydrological/mechanical phenomena in porous media. SPE J. 21, 1–041.
Winterfeld, P.H., Wu, Y.S., 2018. Quantitative characterization of impacts of coupled geomechanics and flow on safe and permanent geological storage of CO2 in fractured aquifers. Colorado School of Mines, Golden, CO (United States) Final Report.
Wu, Y.S., 2015. Multiphase Fluid Flow in Porous and Fractured Reservoirs. Gulf Professional Publishing.
Wu, Y.S., Pruess, K., 1988. A multiple-porosity method for simulation of naturally fractured petroleum reservoirs. SPE Reserv. Eng. 3, 327–336.
Xiong, Y., 2015. Development of a compositional model fully coupled with geomechanics and its application to tight oil reservoir simulation. Ph.D. thesis. Colorado School of Mines.
Yu, W., Lashgari, H.R., Wu, K., Sepehrnoori, K., 2015. CO2 injection for enhanced oil recovery in Bakken tight oil reservoirs. Fuel 159, 354–363.
Yu, W., Zhang, Y., Varavei, A., Sepehrnoori, K., Zhang, T., Wu, K., Miao, J., 2018. Compositional simulation of CO2 huff-n-puff in Eagle Ford tight oil reservoirs with CO2 molecular diffusion, nanopore confinement and complex natural fractures. In: SPE Improved Oil Recovery Conference. Society of Petroleum Engineers.
Zoback, M.D., 2010. Reservoir Geomechanics. Cambridge University Press.